

# EXPERIENCE WITH DNS OF PARTICULATE FLOW USING A VARIANT OF THE IMMERSED BOUNDARY METHOD

Markus Uhlmann

CIEMAT  
Modeling and Numerical Simulation Unit  
Avenida Complutense 22  
28040 Madrid, Spain  
e-mail: [markus.uhlmann@ciemat.es](mailto:markus.uhlmann@ciemat.es)

**Key words:** Particulate Flow, Immersed Boundary Method, Direct Numerical Simulation, Turbulent Channel Flow

**Abstract.** *We perform a grid convergence study for a recently proposed immersed boundary method for DNS of particulate flows with interface resolution [Uhlmann, J. Comput. Phys., 209(2):448–476, 2005]. Two cases of vertical plane Poiseuille flow with suspended heavy particles (with terminal particle Reynolds number  $\geq 100$ ) are considered, in the laminar and in the turbulent flow regimes. The solutions obtained for different spatial refinements while keeping the CFL number constant are analyzed. A convergence rate of approximately  $\Delta x^2$  is determined for the prediction of the particle motion in the laminar shear flow. A quantitative evaluation of the grid-related discrepancies is presented for the time-dependent individual particle velocity, the Lagrangian particle statistics and the Eulerian fluid statistics in the turbulent case.*

## 1 INTRODUCTION

In the past, most direct numerical simulations of particulate flow were based upon the point-particle approach. Whenever the Reynolds number of the flow around the particle exceeds a certain value and/or the particle size is not small compared to the size of the smallest turbulent structures, this simplification is no longer valid and the fluid-solid interface needs to be resolved.

Under these circumstances, an accurate numerical simulation of the dynamics of a particulate flow system presents a considerable challenge even at modest system sizes, because the different phase interfaces are in relative motion to each other. One way to solve this problem efficiently is by using a fixed computational grid and applying the immersed boundary method for imposing the adequate constraints at the internal boundaries.

We have recently proposed a variant of the immersed boundary method<sup>1</sup> which uses a direct formulation of the forcing term (i.e. no feed-back law), thereby allowing for relatively large time steps, while using the discrete delta function formalism<sup>2</sup> for the necessary interpolation and spreading operations of variables from Eulerian to Lagrangian space locations and vice versa. The advantage of this formulation is a substantial reduction of the grid-induced oscillations of the hydrodynamic forces acting upon a particle in motion.

The method has previously been validated in a number of cases involving single particles and pairs of particles, both circular and spherical, as well as a range of flow configurations, with reference to available numerical and experimental data. What has been lacking so far is the demonstration of grid convergence in a case which is directly comparable to our target configuration of turbulent particulate flow in a wall-bounded configuration<sup>3</sup>. In the present article we present two refinement studies for the vertical flow in a plane channel with suspended heavy particles, in the laminar and turbulent flow regimes.

## 2 NUMERICAL METHOD

The Navier-Stokes equations for an incompressible fluid can be written as:

$$\partial_t \mathbf{u} + (\mathbf{u} \cdot \nabla) \mathbf{u} + \nabla p = \nu \nabla^2 \mathbf{u} + \mathbf{f} \quad (1a)$$

$$\nabla \cdot \mathbf{u} = 0 \quad (1b)$$

where  $\mathbf{u}$  is the vector of fluid velocities,  $p$  the pressure normalized with the fluid density and  $\mathbf{f}$  a volume force term. The basic idea of the immersed boundary method is to solve these equations in the entire domain  $\Omega$ , including the space occupied by the solid particles, instead of only considering the interstitial fluid domain  $\Omega_f$ . For this purpose, the force term  $\mathbf{f}$  is introduced and formulated in such a way as to impose a rigid body motion upon the fluid at the locations of the solid particles. The main advantage of this approach lies in the possibility to use a fixed computational grid with a simple structure, allowing for efficient numerical solution techniques to be applied.

In the following we will recall the essential points of our specific formulation of the immersed boundary method<sup>1</sup>. For this purpose, let us write the momentum equation in semi-discrete form:

$$\frac{\mathbf{u}^{n+1} - \mathbf{u}^n}{\Delta t} = \mathbf{rhs}^{n+1/2} + \mathbf{f}^{n+1/2}, \quad (2)$$

where  $\mathbf{rhs}$  regroups the convection term, the pressure gradient and the viscous term, the superscripts denoting the time level. The additional force in (2) can be expressed by simply rewriting the equation<sup>4</sup>:

$$\mathbf{f}^{n+1/2} = \frac{\mathbf{u}^{(d)} - \mathbf{u}^n}{\Delta t} - \mathbf{rhs}^{n+1/2} \quad (3)$$

where  $\mathbf{u}^{(d)}$  is the desired velocity at any grid point where forcing is to be applied (i.e. at a node inside a solid body). Formula (3) is characteristic for direct forcing methods<sup>4,5</sup>, as

opposed to formulations which rely on a feed-back mechanism<sup>6-8</sup>. The drawback of the latter techniques is an often severe restriction of the time step, caused by the time scale of the feed-back law itself. Direct forcing methods, on the other hand, are free from this restriction.

However, problems can arise in practice from the fact that the solid-fluid interface seldomly coincides with the Eulerian grid lines, meaning that interpolation needs to be performed in order to obtain an adequate representation of the interface. Inspired by Peskin's original immersed boundary method<sup>2,9</sup>, we choose to compute the force term at Lagrangian positions attached to the surface of the particles, viz.

$$\mathbf{F}^{n+1/2} = \frac{\mathbf{U}^{(d)} - \mathbf{U}^n}{\Delta t} - \mathbf{RHS}^{n+1/2}, \quad (4)$$

where upper-case letters indicate quantities evaluated at Lagrangian coordinates. Obviously, the velocity in the particle domain  $\mathcal{S}$  is simply given by the solid-body motion,

$$\mathbf{U}^{(d)}(\mathbf{X}) = \mathbf{u}_c + \boldsymbol{\omega}_c \times (\mathbf{X} - \mathbf{x}_c) \quad \mathbf{X} \in \mathcal{S}, \quad (5)$$

as a function of the translational and rotational velocities of the particle,  $\mathbf{u}_c$ ,  $\boldsymbol{\omega}_c$ , and its center coordinates,  $\mathbf{x}_c$ . The two remaining terms on the right hand side of (4) can be collected as

$$\tilde{\mathbf{U}} = \mathbf{U}^n + \mathbf{RHS}^{n+1/2} \Delta t \quad (6)$$

which corresponds to a preliminary velocity obtained without applying a force term. Its Eulerian counterpart,

$$\tilde{\mathbf{u}} = \mathbf{u}^n + \mathbf{rhs}^{n+1/2} \Delta t \quad (7)$$

is evaluated explicitly.

The final element of our method is the transfer of the velocity (and r.h.s. forces) from Eulerian to Lagrangian positions as well as the inverse transfer of the forcing term to the Eulerian grid positions. For this purpose we define a Cartesian grid  $\mathbf{x}_{ijk}$  with uniform mesh width  $\Delta x$  in all three directions. Furthermore, we distribute so-called discrete Lagrangian force points  $\mathbf{X}_l$  (with  $1 \leq l \leq N_L$ ) evenly on the particle surface. Using the regularized delta function formalism of Peskin<sup>2,9</sup>, the transfer can be written as:

$$\tilde{\mathbf{U}}(\mathbf{X}_l) = \sum_{ijk} \tilde{\mathbf{u}}(\mathbf{x}_{ijk}) \delta_h(\mathbf{x}_{ijk} - \mathbf{X}_l) \Delta x^3, \quad (8a)$$

$$\mathbf{f}(\mathbf{x}_{ijk}) = \sum_l \mathbf{F}(\mathbf{X}_l) \delta_h(\mathbf{x}_{ijk} - \mathbf{X}_l) \Delta V_l, \quad (8b)$$

where  $\Delta V_l$  designates the forcing volume assigned to the  $l$ th force point. We use a particular function  $\delta_h$  which has the properties of continuous differentiability, second order accuracy, support of three grid nodes in each direction and consistency with basic properties of the Dirac delta function<sup>10</sup>.

It should be underlined that the force points are distributed on the interface between fluid and solid, and not throughout the whole solid domain. The reason for this is efficiency: the particle-related work currently scales as  $(D/\Delta x)^2$  instead of  $(D/\Delta x)^3$ . The consequences for the efficiency of the forcing due to these two alternative placements of the forcing points have been discussed in a previous study<sup>11</sup>.

The above method has been implemented in a staggered finite-difference context, involving central, second-order accurate spatial operators, an implicit treatment of the viscous terms and a three-step Runge-Kutta procedure for the non-linear part. Continuity in the entire domain  $\Omega$  is enforced by means of a projection method.

The particle motion is determined by the Runge-Kutta-discretized Newton equations for rigid-body motion, which are weakly coupled to the fluid equations.

One step of our algorithm can be summed up as follows:

1. compute the explicit velocity estimation  $\tilde{\mathbf{u}}$
2. transfer  $\tilde{\mathbf{u}}$  to Lagrangian positions at the fluid-solid interfaces
3. compute the force term  $\mathbf{F}$
4. transfer  $\mathbf{F}$  back to Eulerian grid positions, obtaining  $\mathbf{f}$
5. solve Navier-Stokes on the fixed grid with the added force term  $\mathbf{f}$
6. step the equations for particle motion, using the available force/torque.

The entire set of equations has been given elsewhere<sup>1</sup>.

The current algorithm has been coded for execution on parallel machines with distributed memory, using the MPI library. For reasons of efficiency, the Helmholtz problems to be solved during the predictor step are simplified by second-order-accurate approximate factorization and the Poisson problem in the projection step is solved by a multi-grid technique. We use a domain decomposition approach for distributing the Eulerian nodes over a three-dimensional processor grid. Each processor treats the particles momentarily located in its sub-domain. Additionally, the neighbor processors need to contribute to the transfer operations (8) whenever particles happen to overlap sub-domains of the distributed grid. The particle treatment can therefore be described as a “master-and-slave” technique.

Our method has previously undergone extensive testing and validation with reference to available analytic, experimental and numerical data. The most important test cases were the following: (i) Taylor-Green flow in an immersed region<sup>1</sup>; (ii) flow around a stationary and oscillating cylinder<sup>1</sup>; (iii) a freely rotating circular disc in Couette flow<sup>11</sup>; (iv) a single sedimenting circular disc<sup>12</sup>; (v) drafting-kissing-tumbling of two circular discs<sup>1</sup>; (vi) a single fixed sphere in laminar plane channel flow; (vii) sedimentation of a single spherical particle<sup>1</sup>.

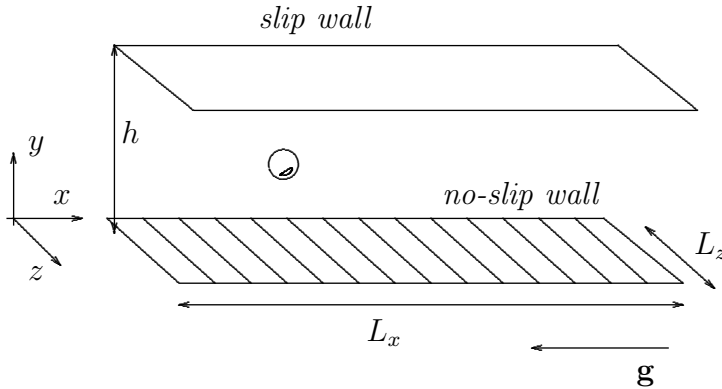


Figure 1: Schematic of the geometry for the case of particulate flow in a plane half-channel.

### 3 RESULTS

In the following we will analyze results from simulations of particulate flow in a vertical plane half-channel configuration (cf. figure 1), bounded by one no-slip wall ( $y = 0$ ,  $\mathbf{u} = 0$ ) and one free-slip surface ( $y = h$ ,  $v = \partial_y u = \partial_y w = 0$ ). The flow field is assumed periodic in the  $x$  and  $z$  directions, with periods of  $L_x$  and  $L_z$ . A constant flow rate is maintained along the  $x$  coordinate (constant bulk velocity,  $U_b = \int_{\Omega} u \, d\mathbf{x} / |\Omega| > 0$ ), while the gravity vector points in the opposite direction ( $g_x < 0$ ).

#### 3.1 The motion of a single heavy particle in vertical laminar channel flow

The initial condition for the carrier phase corresponds to plane Poiseuille flow, viz.

$$v(t=0) = w(t=0) = 0, \quad u(t=0) = \left(1 - \left(\frac{y}{h} - 1\right)^2\right) \frac{3}{2} U_b. \quad (9)$$

The viscosity is adjusted such that the flow is in the laminar regime, with a bulk Reynolds number of  $Re_b = U_b h / \nu = 1000$ .

A single particle with diameter  $D/h = 1/20$  is initially located halfway between the wall and the free-slip surface ( $y_c(t=0) = 0.5h$ ). Its initial translational velocity is matched with the velocity of the fluid at the center position ( $u_c(t=0) = \frac{9}{8} U_b$ ,  $v_c(t=0) = w_c(t=0) = 0$ ) and the angular particle velocity is set to zero ( $\boldsymbol{\omega}_c(t=0) = 0$ ). The density ratio between solid and fluid is set to  $\rho_p / \rho_f = 4.17$ , which means that the Stokes number (defined as  $St = D^2 \rho_p / \rho_f U_b / (18 \nu h)$ ) takes a value of 0.58 for this particle. The non-dimensional gravity is set to  $|\mathbf{g}| D / U_b^2 = 1.1036$ , leading to a terminal particle velocity of  $u_{c,\infty} = 2U_b$ . This latter value corresponds to a terminal particle Reynolds number of  $Re_{D,\infty} = u_{c,\infty} D / \nu \approx 100$ .

The determination of possible equilibrium positions and lift force correlations for particles in shear flows has been widely discussed in the literature<sup>13-17</sup>. However, no theory

grid	$N_x \times N_y \times N_z$	$D/\Delta x$	$N_L$	$\Delta t U_b/h$
$\mathcal{G}_1$	$128 \times 257 \times 128$	12.8	515	$6.67 \cdot 10^{-4}$
$\mathcal{G}_2$	$192 \times 385 \times 192$	19.2	1158	$4.44 \cdot 10^{-4}$
$\mathcal{G}_3$	$256 \times 513 \times 256$	25.6	2059	$2.96 \cdot 10^{-4}$
$\mathcal{G}_4$	$384 \times 769 \times 384$	38.4	4632	$1.98 \cdot 10^{-4}$

Table 1: Grid parameters and time step for the convergence study of a single spherical particle in laminar Poiseuille flow of § 3.1. The lengths of the periods in the streamwise and spanwise directions are  $L_x = 0.5h$  and  $L_z = 0.5h$ . The particle diameter is  $D/h = 1/20$ .

or experimental data is available to our knowledge for the present parameter range (in particular at the present Reynolds number value).

We have performed the simulation in a relatively small domain with streamwise and spanwise periods of  $L_x = L_z = 0.5$  using 4 different grids, corresponding to a sequence of simultaneous grid refinements of all coordinate directions by factors of 1,  $\frac{2}{3}$ ,  $\frac{1}{2}$  and  $\frac{1}{3}$  (cf. table 1). Therefore, the ratio between the particle diameter and the mesh width varies threefold (from 12.8 to 38.4). The time step is reduced proportionally, such that a maximum value of approximately 0.25 for the CFL number is maintained throughout the series.

Figure 2 shows the particle path and velocity in the  $(x, y)$ -plane as computed on the coarsest grid up to time  $t_1 = 8h/U_b$ . Initially, the particle advances in the streamwise direction until the gravitational acceleration has reversed its course, from then on travelling with a negative  $x$ -component of velocity. The particle velocity in the wall-normal direction is at first positive (directed away from the wall) and—after a close encounter with the free-slip surface (without contact)—reverses the sign at  $t \approx 6.5h/U_b$ . The curve for  $v_c$  exhibits some oscillations immediately after the release of the particle and—to a greater extent—for times  $t \geq 7h/U_b$ . The convergence study below will show that this feature is not a numerical artifact. The physical mechanism is, however, unclear at the time being. It can be speculated that it is related to the non-symmetric wake structure which affects the very particle motion since the field is periodic in the streamwise direction with a very short period of only 10 particle diameters.

Let us now turn to the convergence study. Figure 3 compares our results for the particle motion as obtained with the four different grids up to time  $t_2 = 0.978h/U_b$ . It can be observed that the temporal evolution of the translational and angular particle velocity is well represented by all four discretizations. The maximum difference in the streamwise velocity between finest and coarsest grid is below 7% of the maximum value (less than 9% of the bulk velocity), with the coarser grids leading to an over-prediction of the drag, i.e. a slight under-prediction of the particle acceleration. The difference for the wall-normal component is below 1% of the bulk velocity. On the other hand, since the amplitude of this component is two orders of magnitude smaller than the streamwise counterpart, this translates to a difference of up to 53% of its maximum value. However, the main

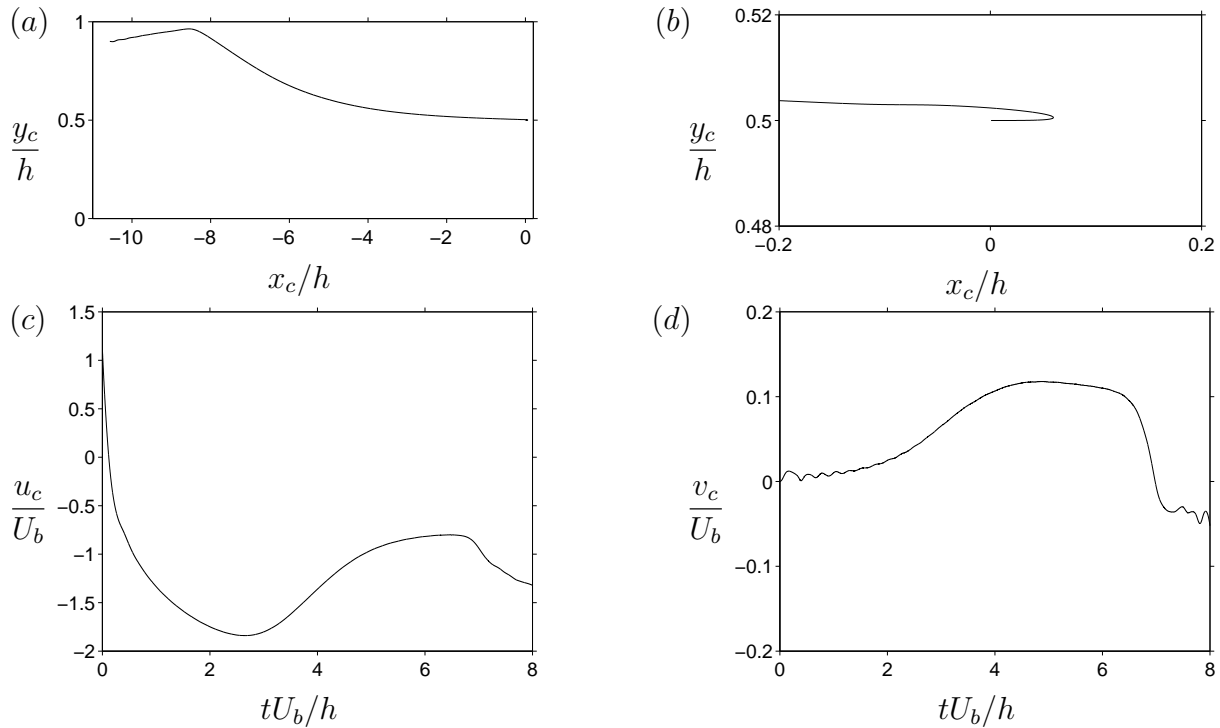


Figure 2: Motion of a single heavy sphere in laminar Poiseuille flow computed with grid  $\mathcal{G}_1$ : (a) Particle path in the  $(x, y)$ -plane; (b) zoom of (a) around the point of release; (c) temporal evolution of the streamwise component of the particle velocity; (d) wall-normal component of the particle velocity. Note that the periodic wrap-around has been eliminated from the  $x$ -coordinate in graphs (a) and (b) for clarity.

feature—the above mentioned oscillation of the wall-normal velocity—is captured by all four grids. Moreover, the period and amplitude of the oscillation of  $v_c$  is consistently predicted; the main difference between the curves in figure 3(b) is a vertical shift. Since the lift force due to shear is directly related to the particle velocity<sup>16</sup> the discrepancy in the wall-normal velocity component can be considered a consequence of the differences in the prediction of the streamwise component. Finally, the spanwise component of the angular velocity shows a similar overall behavior and similar grid-related differences as the wall-normal translation velocity. The remaining components  $(w_c, \omega_{c,x}, \omega_{c,y})$  have been omitted since they remain one order of magnitude smaller than their counterparts.

In order to compute a quantitative measure of the convergence, we define the “error” of a solution on a grid  $\mathcal{G}_i$  with respect to the solution on the finest grid  $\mathcal{G}_4$ :

$$\mathcal{E}_i(\phi_c) = |\phi_c(\mathcal{G}_i) - \phi_c(\mathcal{G}_4)|, \quad (10)$$

where  $\phi_c$  stands for any particle-related quantity. Figure 4 shows the error of the particle velocity components  $u_c$  and  $v_c$  (measured at time  $t = t_2$ ), plotted as a function of the mesh width. A variation approximately proportional to  $\Delta x^2$  can be observed in both graphs. It should be kept in mind here that the convergence rate is in reality not purely spatial, since the time step was simultaneously varied to keep the CFL number constant.

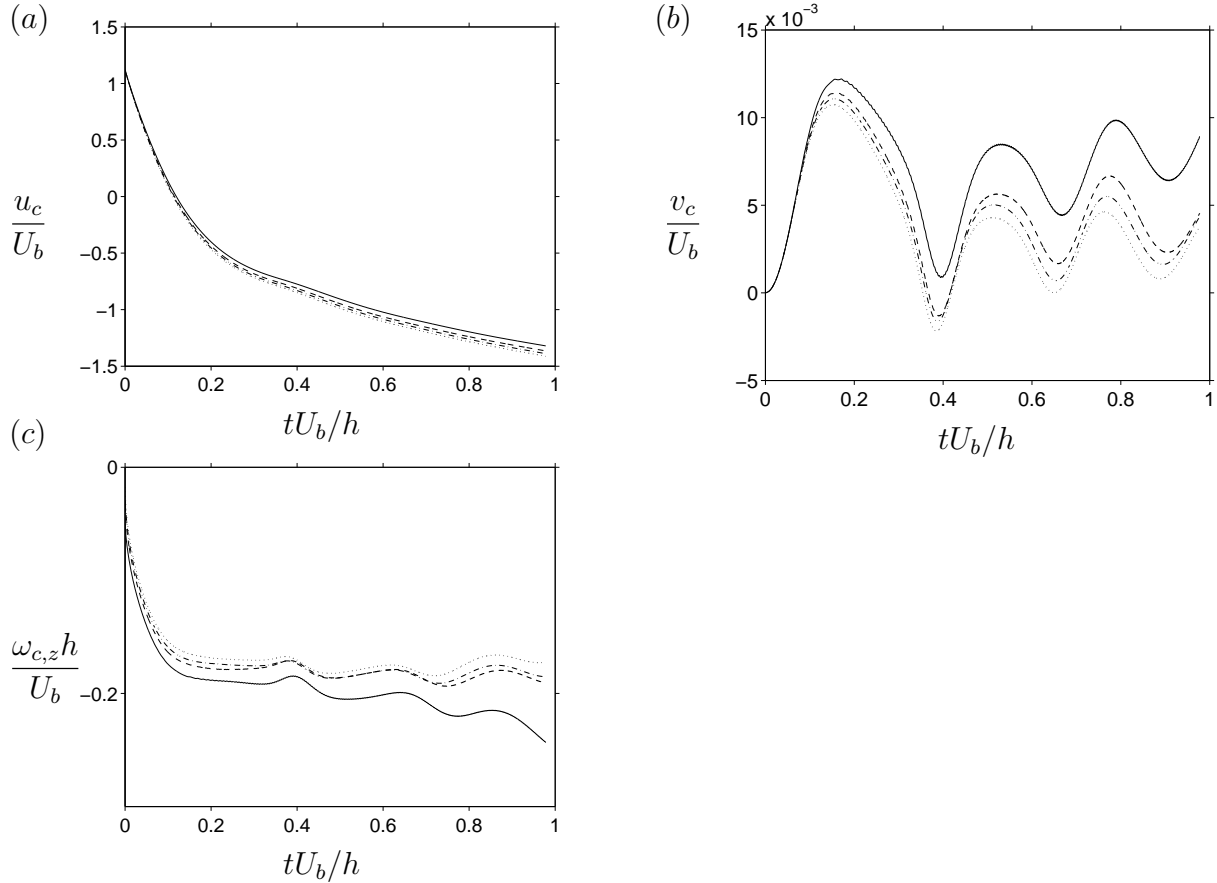


Figure 3: Temporal evolution of the particle velocities in case § 3.1, computed with different grids: (a) streamwise component; (b) wall-normal component; (c) spanwise component of the angular velocity. Line styles: —,  $\mathcal{G}_1$ ; ---,  $\mathcal{G}_2$ ; -·-,  $\mathcal{G}_3$ ; ····,  $\mathcal{G}_4$ .

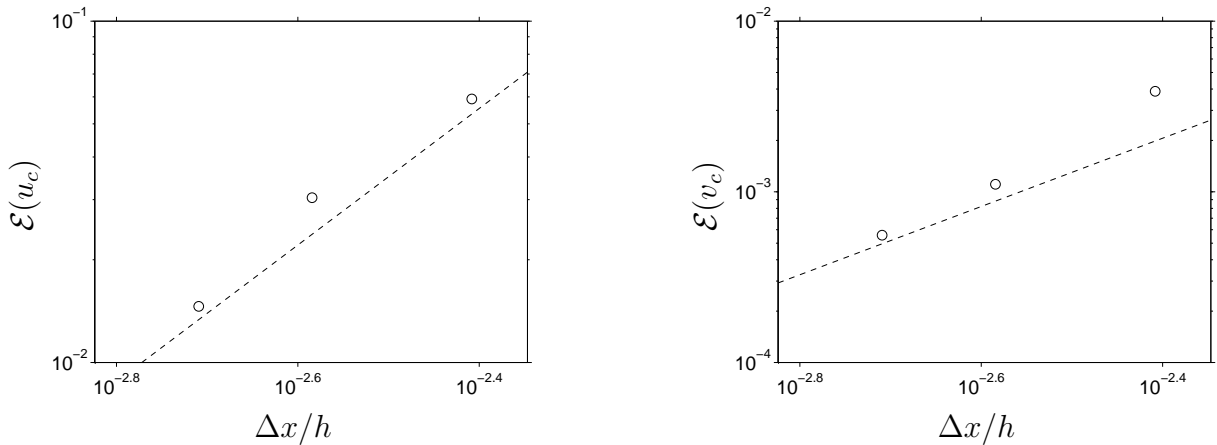


Figure 4: Error relative to the solution on the finest grid for the data shown in figure 3 at time  $t_2 = 0.978h/U_b$ . The dashed line indicates a slope of  $\Delta x^2$  in both cases.

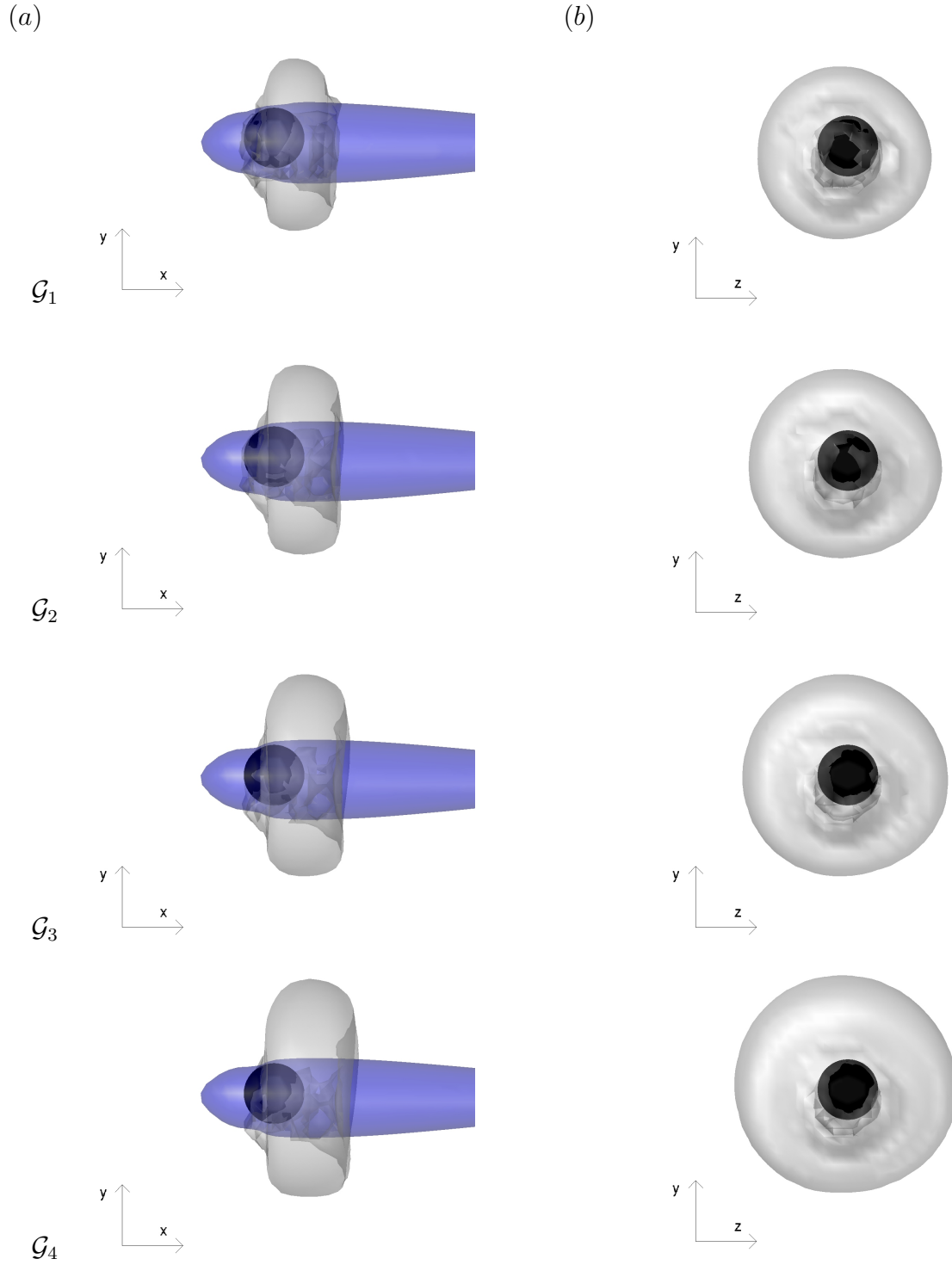


Figure 5: View of the near-field around the particle of § 3.1 at time  $t_2 = 0.978h/U_b$  as computed with the four different grids  $\mathcal{G}_i$ : (a) side view; (b) front view. The blue surface in (a) corresponds to a negative value of the streamwise velocity fluctuation ( $u' = -0.9U_b$ ). The grey surface in both (a) and (b) indicates intense vortical structures by means of the  $\lambda_2$ -criterion<sup>18</sup>.

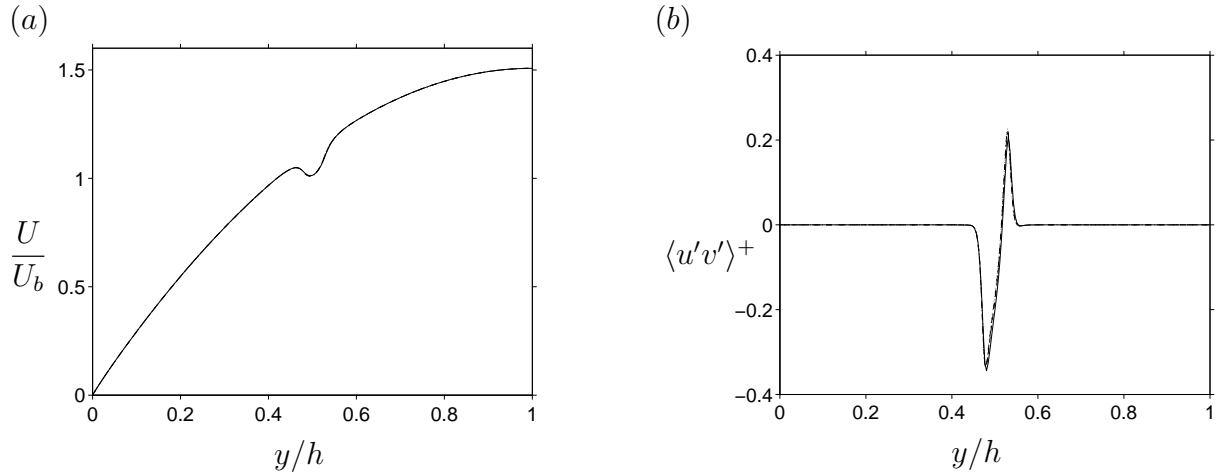


Figure 6: Fluid statistics up to time  $t_2$  for case § 3.1: (a) mean fluid velocity; (b) Reynolds stress. Line styles as in figure 3.

grid	$N_x \times N_y \times N_z$	$D/\Delta x$	$N_L$	$\Delta t U_b/h$
$\mathcal{G}_1$	$512 \times 257 \times 256$	12.8	515	$2.27 \cdot 10^{-3}$
$\mathcal{G}_2$	$768 \times 385 \times 384$	19.2	1158	$1.51 \cdot 10^{-3}$
$\mathcal{G}_3$	$1024 \times 513 \times 512$	25.6	2059	$1.14 \cdot 10^{-3}$

Table 2: Grid parameters for the convergence study of four spherical particles suspended in turbulent flow in a plane half-channel of § 3.2. The lengths of the periods in the streamwise and spanwise directions are  $L_x = 2h$  and  $L_z = h$ . The particle diameter is  $D/h = 1/20$ .

The plots in figure 5 illustrate the flow field in proximity of the particle for  $t = t_2$  by means of isosurfaces of the streamwise velocity fluctuation  $u'$  (where  $\mathbf{u}' = \mathbf{u} - U$ ,  $U(y) = \langle u \rangle$ ,  $\langle \cdot \rangle$  designates the average over time and wall-parallel planes) and vortical structures educed by the  $\lambda_2$ -criterion<sup>18</sup>. For the four grids, a good match of the shape of the wake and the attached vortex ring can be observed.

Finally, let us consider the fluid statistics accumulated over the interval  $t \in [0, t_2]$ . Figure 6 shows the profiles of the mean fluid velocity  $U$  and the Reynolds stress  $\langle u'v' \rangle$ . For both quantities (as well as for the other stress components which have been omitted) we obtain a near-perfect agreement with all four discretizations.

### 3.2 Four heavy particles in vertical turbulent channel flow

In this case the fluid motion is fully turbulent with a bulk Reynolds number of  $Re_b = 2700$  (friction-velocity-based Reynolds number  $Re_\tau \approx 180$ ). The initial flow field was generated by a spectral simulation in the full domain (i.e. with  $y \in [0, 2h]$  and two no-slip walls), then spectrally interpolated to the present half-channel ( $y \in [0, h]$ ). The lengths of the streamwise and spanwise period measure  $L_x = 2h$  and  $L_z = h$ , respectively, which

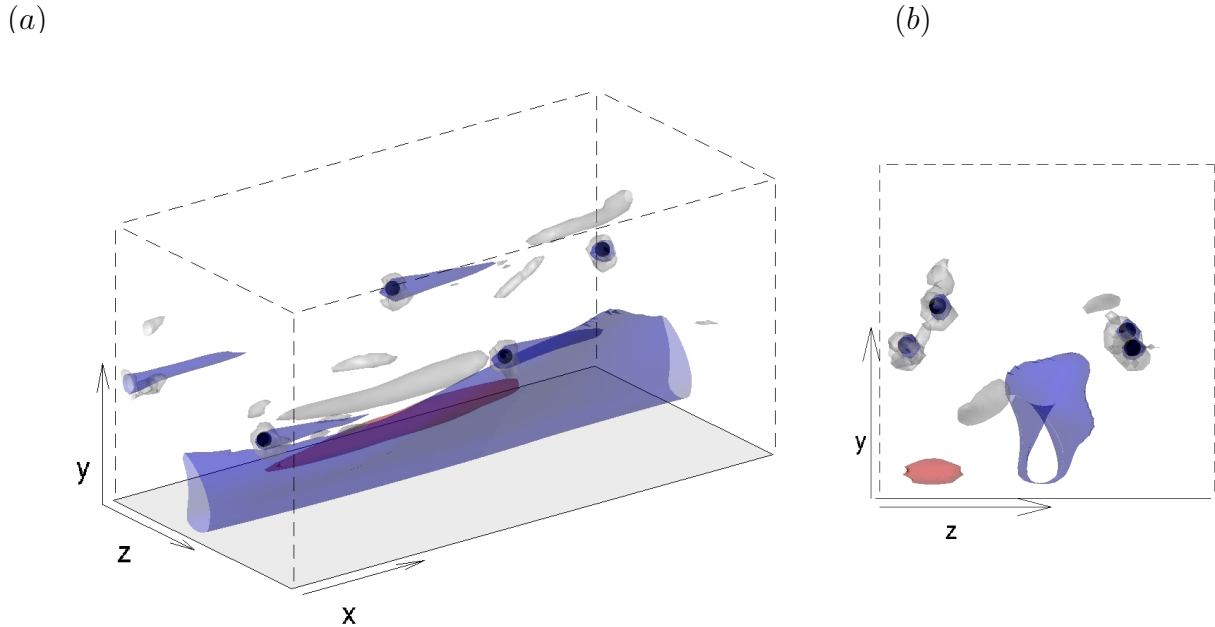


Figure 7: The flow field of case § 3.2 at time  $t_2 = 3.58h/U_b$  as computed with the grid  $\mathcal{G}_1$ : (a) perspective view; (b) view into the mean flow direction. The blue/red surfaces correspond to values of the streamwise velocity fluctuation of  $u' = \pm 0.28U_b$  (blue is negative). The grey surface indicates intense vortical structures by means of the  $\lambda_2$ -criterion<sup>18</sup>.

is sufficient in order to maintain turbulence at the present Reynolds number.

Four particles were simultaneously introduced into the flow at  $t = 0$ , widely-spaced apart in the plane  $y = 0.5h$ . As in § 3.1, the particle diameter measures  $D/h = 1/20$  (in wall units:  $D^+ = 9$ ), the initial translational particle velocities are matched with the velocity of the fluid at the respective center positions and the initial angular particle velocities are set to zero. The density ratio is set to  $\rho_p/\rho_f = 2.2077$ , i.e. the Stokes number takes a value of  $St = 0.83$ ; the non-dimensional gravity is set to  $|\mathbf{g}|D/U_b^2 = 0.6136$  ( $u_{c,\infty} \approx U_b$ ,  $Re_{D,\infty} \approx 136$ ). These values were chosen in accordance with one of our large-scale simulations of particulate channel flow<sup>3</sup>.

We have tested three different discretizations, using the mesh widths of the first three grids chosen in § 3.1 (cf. table 2). Therefore, the values in wall units are  $\Delta x^+ = 0.7, 0.47, 0.35$  for the present case. It was established in an independent simulation that the coarsest grid is sufficient for the simulation of the single-phase turbulent flow at the present Reynolds number. Here the time step was adjusted such that the CFL number was maintained at approximately 0.725 in all three runs. Note that this value is about three times larger than in the laminar case of § 3.1.

Figure 7 shows a snapshot of the flow at time  $t_2 = 3.58h/U_b$ . At this moment the field is characterized by a nearly straight low-speed streak which is flanked by a shorter high-speed streak, while a streamwise vortex is situated in between and slightly above the

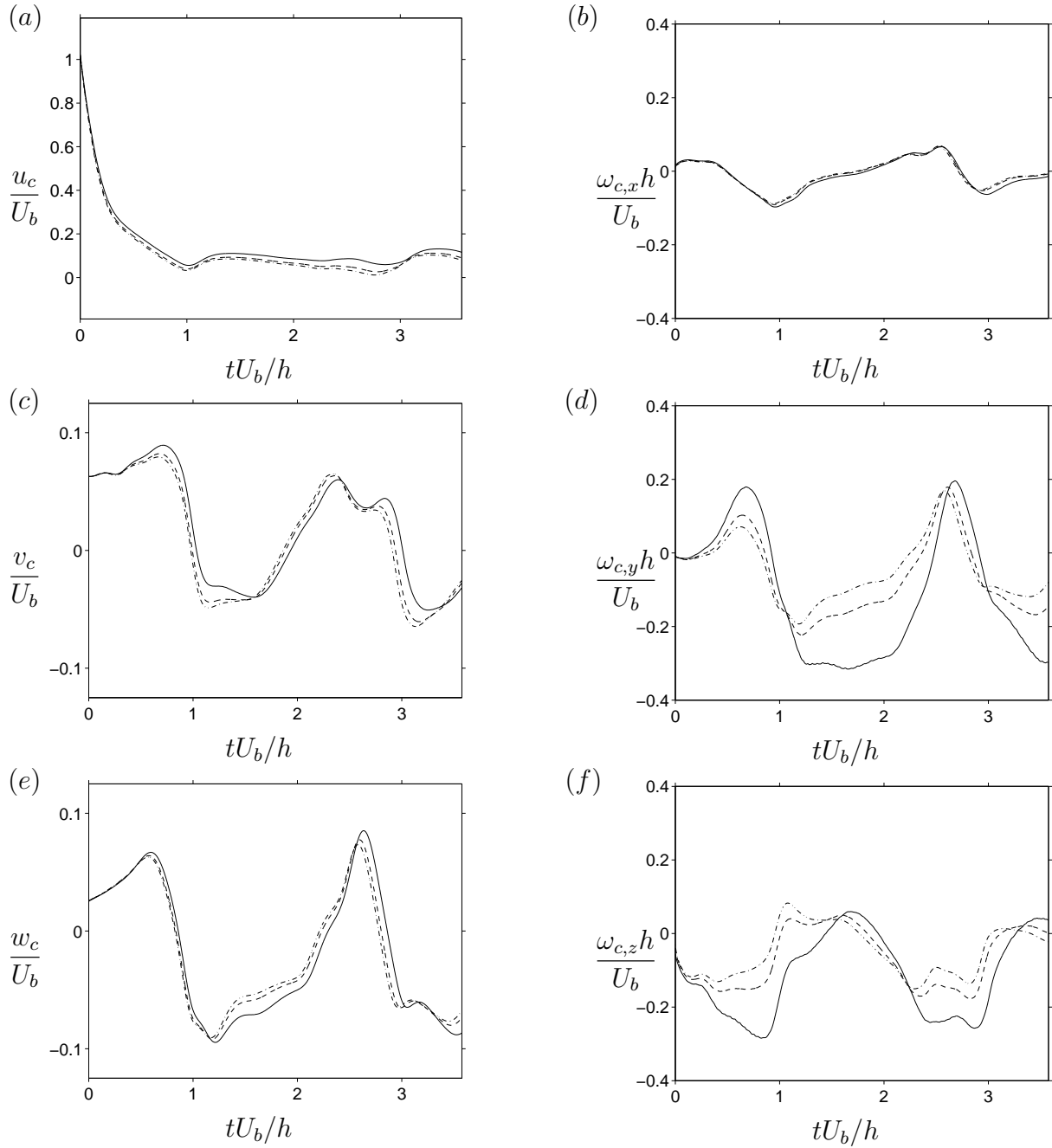


Figure 8: Temporal evolution of the motion of one of the four particles of case § 3.2 as computed with three different grids: (a), (c), (e) components of the translational particle velocity; (b), (d), (f) components of the angular particle velocity. Line styles: —,  $\mathcal{G}_1$ ; ----,  $\mathcal{G}_2$ ; - · -,  $\mathcal{G}_3$ .

two structures. The velocity perturbations in the wakes of the particles are of comparable magnitude to the streak intensity.

The evolution of the velocity of the particle motion in these turbulent surroundings is

shown in figure 8, where the solutions computed with the three discretizations are compared. For clarity, the graphs show data for one particle only, the conclusions from the other results being very similar (the other plots have been omitted). The curves for the translational particle velocity components  $u_c$ ,  $v_c$ ,  $w_c$  obtained with the three grids match to within 8.3% of the bulk velocity. It is worth noting that even the result computed on the coarsest grid exhibits all the features of the refined runs. Concerning the angular particle velocity (figure 8d-f), we observe a higher sensitivity to the grid refinement with differences of up to 4%, 40% and 23% of the “bulk shear” ( $U_b/h$ ) for the  $x$ ,  $y$ ,  $z$ -components. Between the two finer grids  $\mathcal{G}_2$  and  $\mathcal{G}_3$  these latter differences reduce to below 1.2%, 10.6% and 6.5%.

It should be recalled that small perturbations can amplify exponentially in the turbulent flow, and even two very well resolved simulations will yield diverging states eventually. What is expected of a converged simulation, however, is that the relevant statistics remain unaffected by additional refinement. The ideal way to verify grid independence of a result would therefore be to integrate the problem up to convergence of the statistics on all grids. This method is unfortunately at present prohibitively expensive, in particular, since the necessary time intervals are extremely large in dilute suspension flows. As an alternative, we will consider the limited statistics accumulated for the period  $t \in [0, t_2]$  and perform an average over the four particles.

For this purpose let us define the Lagrangian two-time auto-correlation along particle paths as follows:

$$R(\phi_c, \tau) = \frac{1}{\langle \phi_c \rangle_t^2} \frac{1}{N_p} \sum_{i=1}^{N_p} \langle \phi_c^{(i)}(t) \cdot \phi_c^{(i)}(t + \tau) \rangle_t, \quad (11)$$

where  $N_p = 4$  is the number of particles,  $\langle \cdot \rangle_t$  designates the time average and  $\phi_c$  stands for any particle-related quantity. Figure 9 shows the correlation data for translational and angular velocity. The streamwise velocity component exhibits an exponential-like decay, while all other translational and angular velocity components reach a minimum with negative value for separations of approximately  $\tau = 1h/U_b$  before increasing again. The results obtained on all three grids reproduce these features with reasonable accuracy, with the largest differences observed for the  $x$ - and  $z$ -component of the angular velocity. Table 3 gives the maximum values of these differences with respect to the finest grid. It can be seen that the error is at most 10.4% for the translational velocity components on the coarsest grid and that it drops below 3.5% on the grid  $\mathcal{G}_2$ . For the angular velocity the maximum error on the coarse grid is 32%, dropping to below 15% on grid  $\mathcal{G}_2$ .

The statistics for the carrier phase are shown in figure 10. First, let us point out the perfect agreement of the fluid statistics away from the location of the particles ( $y_c \approx 0.5h$ ), which confirms the adequacy of the coarsest grid with respect to the single-phase turbulent flow. Second, we observe a near-perfect match of the curves for all three grids even in the vicinity of the particle locations for the mean velocity as well as the stresses. An exception is the normal stress in the streamwise direction  $\langle u'u' \rangle$ , where we obtain somewhat larger

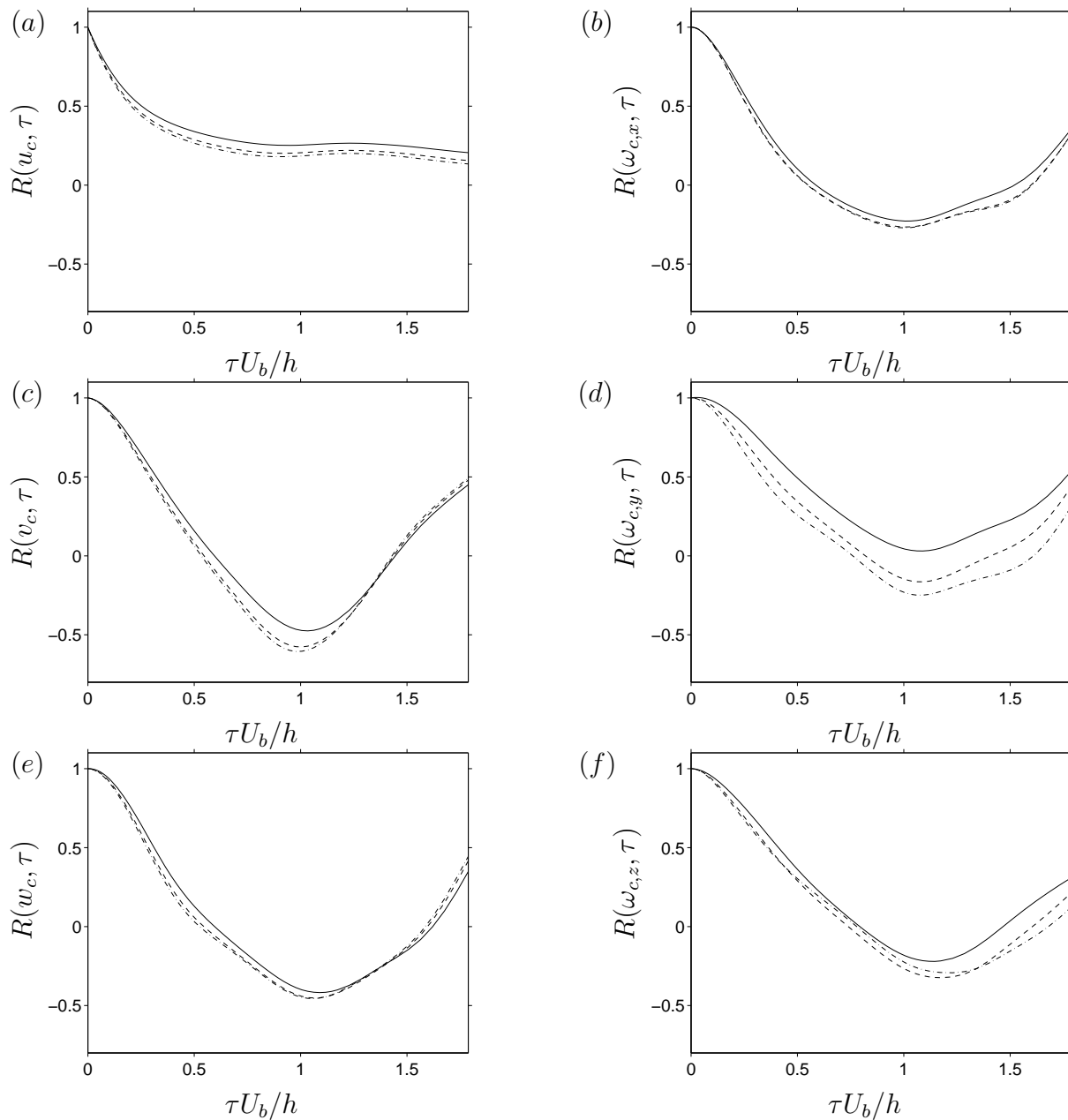


Figure 9: Lagrangian two-time autocorrelations (averaged over all 4 particles) as a function of the temporal separation  $\tau$  for case § 3.2, as computed with three different grids: (a), (c), (e) components of the translational particle velocity ; (b), (d), (f) components of the angular particle velocity. Line styles as in figure 8.

relative differences of less than 7% on the coarsest grid (less than 2% on grid  $\mathcal{G}_2$ ).

	$R(u_c)$	$R(v_c)$	$R(w_c)$	$R(\omega_{c,x})$	$R(\omega_{c,y})$	$R(\omega_{c,z})$
$\mathcal{E}_1$	0.076	0.155	0.104	0.089	0.319	0.217
$\mathcal{E}_2$	0.023	0.035	0.029	0.009	0.149	0.090

Table 3: Maximum “error” (as defined in 10) of the Lagrangian autocorrelation data for the different quantities plotted in figure 9.

## 4 CONCLUSIONS

We have performed a convergence study of a recently proposed method for interface-resolved DNS of particulate flow<sup>1</sup>. Two cases of vertical plane Poiseuille flow were considered. In the first one, the fluid flow was laminar and the motion of a single heavy particle with a terminal Reynolds number of 100 and a Stokes number of 0.58 was simulated. In the second case, the flow was turbulent and four particles (with  $Re_{D,\infty} = 136$ ,  $St = 0.83$ ) were tracked.

The laminar case has allowed us to measure the convergence rate of the predictions for the unsteady particle velocity which was found to behave as  $\Delta x^2$ . The fluid statistics were captured with excellent accuracy even by the coarsest of the four grids, which uses 12.8 mesh widths for the representation of the particle diameter (equivalently 515 interpolation points on the particle’s surface). Additional visualizations have confirmed that the representation of the wake structure on all four grids was in very good agreement.

The turbulent case, where the streak intensity was of comparable magnitude as the intensity of the fluctuations in the wake of the particles, is a more stringent test of the discretization due to the presence of a wide spectrum of time and length scales in the carrier phase. We have analyzed the velocity evolution along individual particle paths as well as the Lagrangian particle statistics and the Eulerian fluid statistics obtained by simulations on the three coarsest spatial discretizations of the laminar case (at a larger time step with  $CFL \approx 0.725$ ). It was found that all three grids yield a representation of the particle and fluid motion which is in good agreement, with local differences between the coarse-grid and fine-grid results below 8.3% for the translational particle velocity and below 7% for the fluid statistics. The most delicate point is the prediction of the angular particle velocity, where we have observed that the coarsest grid can lead to local deviations from the fine grid result of up to 40% of the bulk shear for individual components. This figure is reduced to 10.6% for the second coarsest grid.

In the present study we have established the convergence of the solution for particulate (laminar and turbulent) channel flow with the refinement of the discretization. Our results should provide a guide for the selection of a particular computational grid for future simulations in a comparable parameter range.

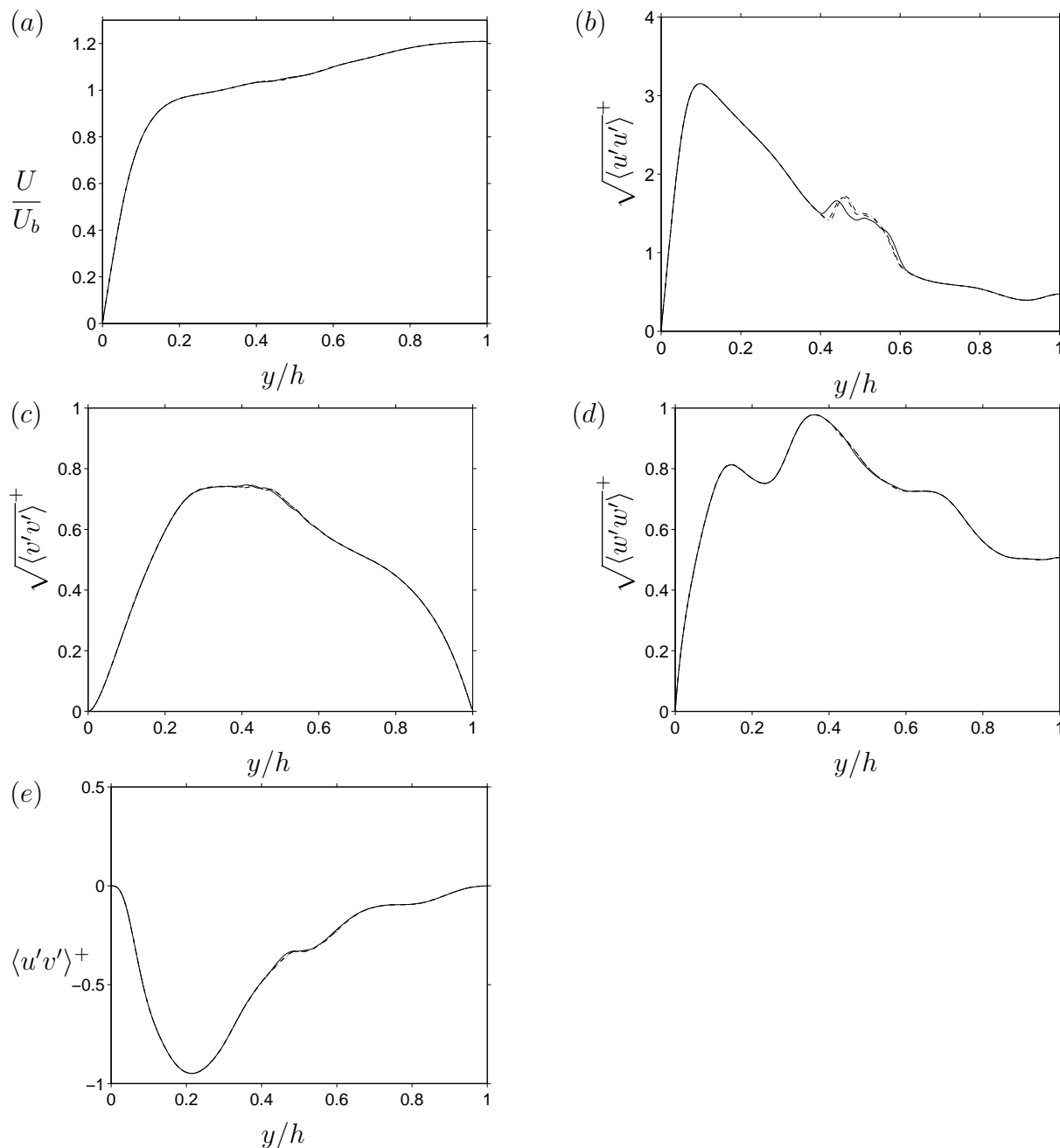


Figure 10: Fluid statistics up to time  $t_2$  for case § 3.2 as computed with three different grids: (a) mean velocity; (b) streamwise fluctuations; (c) wall-normal fluctuations; (d) spanwise fluctuations; (e) Reynolds stress. Line styles as in figure 8.

## ACKNOWLEDGEMENTS

This work was supported by the Spanish Ministry of Education and Science under the Ramón y Cajal program (contract DPI-2002-040550-C07-04) and through grant ENE2005-

09190-C04-04/CON.

## References

- [1] M. Uhlmann. An immersed boundary method with direct forcing for the simulation of particulate flows. *J. Comput. Phys.*, 209(2):448–476, 2005.
- [2] C.S. Peskin. The immersed boundary method. *Acta Numerica*, 11:479–517, 2002.
- [3] M. Uhlmann. DNS of finite-size heavy particles in vertical turbulent channel flow. *Bulletin Am. Phys. Soc.*, 50(9):133, 2005.
- [4] E.A. Fadlun, R. Verzicco, P. Orlandi, and J. Mohd-Yusof. Combined immersed-boundary finite-difference methods for three-dimensional complex flow simulations. *J. Comput. Phys.*, 161:35–60, 2000.
- [5] J. Kim, D. Kim, and H. Choi. An immersed-boundary finite-volume method for simulations of flow in complex geometries. *J. Comput. Phys.*, 171:132–150, 2001.
- [6] D. Goldstein, R. Handler, and L. Sirovich. Modeling a no-slip boundary with an external force field. *J. Comput. Phys.*, 105:354–366, 1993.
- [7] K. Höfler and S. Schwarzer. Navier-Stokes simulation with constraint forces: Finite-difference method for particle-laden flows and complex geometries. *Phys. Rev. E*, 61(6):7146–7160, 2000.
- [8] M.-C. Lai and C.S. Peskin. An immersed boundary method with formal second-order accuracy and reduced numerical viscosity. *J. Comput. Phys.*, 160:705–719, 2000.
- [9] C.S. Peskin. *Flow patterns around heart valves: A digital computer method for solving the equations of motion*. PhD thesis, Albert Einstein College of Medicine, 1972.
- [10] A.M. Roma, C.S. Peskin, and M.J. Berger. An adaptive version of the immersed boundary method. *J. Comput. Phys.*, 153:509–534, 1999.
- [11] M. Uhlmann. An improved fluid-solid coupling method for DNS of particulate flow on a fixed mesh. In M. Sommerfeld, editor, *Proc. 11th Workshop Two-Phase Flow Predictions*, Merseburg, Germany, 2005. Universität Halle. ISBN 3-86010-767-4.
- [12] M. Uhlmann. New results on the simulation of particulate flows. Technical Report No. 1038, CIEMAT, Madrid, Spain, 2004. ISSN 1135-9420.
- [13] G. Segré and A. Silberberg. Behaviour of macroscopic rigid spheres in Poiseuille flow. Part 2. Experimental results and interpretation. *J. Fluid Mech.*, 14:136–157, 1962.

- [14] J.A. Schonberg and E.J. Hinch. Inertial migration of a sphere in Poiseuille flow. *J. Fluid Mech.*, 203:517–524, 1989.
- [15] E.S. Asmolov. The inertial lift on a spherical particle in a plane Poiseuille flow at large channel Reynolds number. *J. Fluid Mech.*, 381:63–87, 1999.
- [16] D.D. Joseph and D. Ocando. Slip velocity and lift. *J. Fluid Mech.*, 454:263–286, 2002.
- [17] J.-P. Matas, J.F. Morris, and E. Guazzelli. Inertial migration of rigid spherical particles in Poiseuille flow. *J. Fluid Mech.*, 515:171–195, 2004.
- [18] J. Jeong, F. Hussain, W. Schoppa, and J. Kim. Coherent structures near the wall in a turbulent channel flow. *J. Fluid Mech.*, 332:185–214, 1997.